A&A 640, A54 (2020)
https://doi.org/10.1051/0004-6361/202037997

Astronomy & Astrophysics

Photometry and high-resolution spectroscopy of comet 21P/Giacobini-Zinner during its 2018 apparition*

Y. Moulane[1,2,3], E. Jehin[2], P. Rousselot[4], J. Manfroid[2], Y. Shinnaka[5], F. J. Pozuelos[2], D. Hutsemékers[2], C. Opitom[1,6], B. Yang[1], and Z. Benkhaldoun[3]

[1] European Southern Observatory, Alonso de Cordova 3107, Vitacura, Santiago, Chile
[2] Space sciences, Technologies & Astrophysics Research (STAR) Institute, University of Liège, Liège, Belgium
e-mail: youssef.moulane@doct.uliege.be
[3] Oukaimeden Observatory, High Energy Physics and Astrophysics Laboratory, Cadi Ayyad University, Marrakech, Morocco
[4] Institut UTINAM UMR 6213, CNRS, Univ. Bourgogne Franche-Comté, OSU THETA, BP 1615, 25010 Besançon Cedex, France
[5] Koyama Astronomical Observatory, Kyoto Sangyo University, Motoyama, Kamigamo, Kita-ku, Kyoto 603-8555, Japan
[6] Institute for Astronomy, University of Edinburgh, Royal Observatory, Edinburgh EH9 3HJ, UK

Received 20 March 2020 / Accepted 8 June 2020

ABSTRACT

We report on photometry and high-resolution spectroscopy of the chemically peculiar Jupiter-family comet (hereafter JFC) 21P/Giacobini-Zinner. Comet 21P is a well-known member of the carbon-chain-depleted family, but also displays a depletion of amines. We continuously monitored the comet over more than seven months with the two TRAPPIST telescopes (TN and TS), covering a wide heliocentric distance range from 1.60 au inbound to 2.10 au outbound with a perihelion at 1.01 au on September 10, 2018. We computed and followed the evolution of the dust- (represented by $Af\rho$) and gas-production rates of the daughter species OH, NH, CN, C_3, and C_2 and their relative abundances to OH and to CN over the cometary orbit. We compared them to those measured in the previous apparitions. The activity of the comet and its water production rate reached a maximum of $(3.72 \pm 0.07) \times 10^{28}$ mol s^{-1} on August 17, 2018 ($r_h = 1.07$ au), 24 days before perihelion. The peak value of $A(0)f\rho$ was reached on the same date (1646 ± 13) cm in the red filter. Using a sublimation model for the nucleus, we constrained the active surface of the nucleus using the slow-rotator model. The abundance ratios of the various species are remarkably constant over a wide range of heliocentric distances before and after perihelion, showing a high level of homogeneity of the ices in the surface of the nucleus. The behaviour and level of the activity of the comet is also remarkably similar over the last five orbits. In the coma dust colour, 21P shows reflective gradients similar to JFCs. We obtained a high-resolution spectrum of 21P with UVES at ESO Very Large Telescope one week after perihelion. Using the CN B-X (0, 0) violet band, we measured $^{12}C/^{13}C$ and $^{14}N/^{15}N$ isotopic ratios of 100 ± 10 and 145 ± 10, respectively, both in very good agreement with the ratios commonly found in comets. We measured an ortho-para abundance ratio of NH_3 of 1.16 ± 0.02, corresponding to a nuclear spin temperature of $T_{spin} = 27 \pm 1$ K, which is similar to other comets. While the abundance ratios in the gaseous coma reveal a peculiar composition, the isotopic and ortho-to-para ratios appear entirely normal. We performed a dynamical simulation of 21P and found that it is likely a young member of the JFC population. We favour a pristine composition scenario to explain the chemical peculiarities of this comet.

Key words. comets: general – comets: individual: 21P/Giacobini-Zinner – techniques: photometric – techniques: spectroscopic

1. Introduction

Comet 21P/Giacobini-Zinner (hereafter 21P) is a Jupiter-family comet (JFC) with a short period of 6.5 yr. 21P was discovered in 1900 by Michel Giacobini and was rediscovered by Ernst Zinner in 1913[1]. After its discovery, 21P was observed in most of its apparitions, and many photometric and spectroscopic measurements were reported. In September 1985, 21P was the first comet visited by the International Cometary Exporer (ICE) spacecraft to study the interaction between the solar wind and the cometary atmosphere (Von Rosenvinge et al. 1986; Scarf et al. 1986). 21P is also known as the parent body of the Draconids meteor shower (Beech 1986; Egal et al. 2019). Many spectroscopic-photometric studies at various wavelength ranges have been performed since its discovery (Schleicher et al. 1987; Cochran & Barker 1987; Fink & Hicks 1996; Weaver et al. 1999; Lara et al. 2003; Combi et al. 2011), including production rate measurements and atomic and molecular abundances. 21P is the prototype of depleted comets in C_2 and C_3 with respect to CN and to OH (Schleicher et al. 1987; A'Hearn et al. 1995). The relative abundances of C_2 and C_3 are about five and ten times lower than those measured in typical comets (A'Hearn et al. 1995). 21P was found to also be depleted in NH (Schleicher et al. 1987; Kiselev et al. 2000) and NH_2 (Konno & Wyckoff 1989; Beaver et al. 1990; Fink 2009).

The physical properties of 21P were investigated in the previous apparitions. Its nucleus size is not well determined; the average estimate of its radius is about 1–2 km (Tancredi et al. 2000; Królikowska et al. 2001; Pittichová et al. 2008). Its rotation period is not well constrained; a wide range from 9.5 to 19 h was estimated (Leibowitz & Brosch 1986). The activity of 21P has shown an asymmetric light curve with respect to perihelion in the previous apparitions. In 1985, the production rates pre-perihelion were twice higher than post-perihelion at heliocentric distances of 1.0–1.5 au (Schleicher et al. 1987). The highest gas and dust

* Based on observations collected at the European Southern Observatory under ESO program 2101.C-5051.
[1] https://ssd.jpl.nasa.gov/sbdb.cgi?sstr=21P;old=0;orb=0;cov=0;log=0;cad=0#discovery

production was observed about one month before perihelion for the previous apparitions (Schleicher et al. 1987; Hanner et al. 1992; Lara et al. 2003). Both its unusual composition and the behaviour of its activity during multiple apparitions make 21P an object of great interest. In addition, as it is the parent body of the Draconids, a study of its dust properties might be valuable. The 2018 apparition was very favourable for ground-based observations because the comet was close to both the Sun and Earth at the same time and reached high elevation. Many observed the comet again for the 2018 return using various advanced instrumentation (IR and optical spectrographs on large telescopes) in order to better understand these peculiarities.

This work is organised as follows: after the introduction and historical background given in Sect. 1, we describe the observing circumstances and the reduction process of images obtained with the Transiting Planets and Planetesimals Small Telescope (TRAPPIST) and spectra obtained with UVES at the Very Large Telescope (VLT) in Sect. 2. In Sect. 3 we compute the production rates and discuss the gas and dust activity pre- and post-perihelion as well as the properties of the dust. The relative molecular abundances and their evolution with respect to the heliocentric distance are discussed in Sect. 4 and compared to the IR abundances of the mother species. In Sect. 5 we present the nitrogen and carbon isotopic ratios and the NH_2 (and NH_3) ortho-para ratio derived from the UVES high-resolution spectrum. In Sect. 6 we investigate the dynamical evolution of comet 21P within the last 10^5 yr. Discussion of the chemical composition of 21P and the possible scenarios of its depletion in carbon species are given in Sect. 7. The summary and conclusions are given in Sect. 8.

2. Observation and data reduction

2.1. Photometry (TRAPPIST)

We started monitoring 21P with TRAPPIST-North (hereafter TN) at the beginning of June 2018 when the comet was at 1.55 au from the Sun. The comet was then observed from the Southern Hemisphere with TRAPPIST-South (hereafter TS) from the beginning of September 2018. The pair of TRAPPIST telescopes (Jehin et al. 2011) is very useful in this case as it allowed a continuous monitoring of the comet before and after perihelion. We collected images with the cometary HB narrow-band filters (Farnham et al. 2000) to measure the production rates of the radicals OH, NH, CN, C_3, and C_2. We also acquired images with the dust-continuum filters *BC*, *GC*, and *RC* for blue, green, and red (Farnham et al. 2000). We used the broad-band filters *B*, *V*, *Rc*, and *Ic* (Bessell 1990) to compute the $Af\rho$ parameter, which is a proxy of the dust production rate (A'Hearn et al. 1984), and to derive the dust colours.

Throughout the passage of the comet, we made a high-cadence monitoring of 21P with images taken about twice a week. On photometric nights, we also obtained long series of observations with the gas narrow-band filters, especially CN and C_2 filters, to measure the variations in production rates during the same night that are caused by the rotation of the nucleus. We chose the exposure time of the different filters depending on the brightness of the comet. We used exposure times between 60 and 240 s for the broad-band filters and between 600 and 1500 s for the narrow-band filters. Observational circumstances and the number of sets of each filter are summarised in Table A.1. We started to collect data three months before perihelion to four months after perihelion. The comet reached perihelion on September 10, 2018, at a heliocentric distance of 1.01 au and a geocentric distance of 0.39 au. In total, the comet was observed on 50 different nights with both telescopes, 13 nights before perihelion and 37 nights after. We used the same procedures as described in our previous papers (e.g. Opitom et al. 2015a; Moulane et al. 2018 and references therein) to reduce the data and to perform the flux calibration. To compute the production rates, we converted the flux of different gas species into column densities and adjusted their profiles with a Haser model (Haser 1957). This simple model, which is widely used, is based on a number of assumptions. Outgassing is assumed to be isotropic, and the gas has a constant radial velocity of 1 km s^{-1}. Parent molecules emitted by the nucleus decay by photodissociation to produce the observed daughter molecules. The model adjustment was performed at a physical distance of 10 000 km from the nucleus. Table 1 shows the scale lengths and *g*-factors of different molecules at 1 au scaled by r_h^{-2}. More details about the Haser model and its parameters are given in our previous works (see Moulane et al. 2018 and references therein). We would like to point out that we used the same parameters as Schleicher & Knight (2018) for the previous apparitions of 21P. We derived the $Af\rho$ parameter, a proxy for the dust production (A'Hearn et al. 1984), from the dust profiles in the cometary dust continuum *BC*, *GC*, and *RC* filters and the broad-band *Rc* and *Ic* filters. It was computed at 10 000 km from the nucleus and corrected for the phase-angle effect according to the phase function normalised at $\theta = 0°$ derived by D. Schleicher[2].

Table 1. Scale lengths and fluorescence efficiency of different molecules at 1 au scaled by r_h^{-2}.

Molecules	Parent (km)	Daughter (km)	*g*-factors (erg s^{-1} mol^{-1})
OH(0,0)	2.4×10^4	1.6×10^5	1.49×10^{-15}
NH(0,0)	5.0×10^4	1.5×10^5	6.27×10^{-14}
CN($\Delta\upsilon = 0$)	1.3×10^4	2.1×10^5	2.62×10^{-13}
C_3($\lambda = 4050$ Å)	2.8×10^3	2.7×10^5	1.00×10^{-12}
C_2($\Delta\upsilon = 0$)	2.2×10^4	6.6×10^4	4.50×10^{-13}

Notes. The scale lengths are equivalent to the lifetimes of molecules as we used a constant radial velocity of 1 km s^{-1} (A'Hearn et al. 1995). The fluorescence efficiency is taken from Schleicher's website (https://asteroid.lowell.edu/comet/gfactor.html).

2.2. Spectroscopy (UVES/VLT)

We obtained one spectrum of comet 21P with the Ultraviolet-Visual Echelle Spectrograph (UVES) mounted on the Unit 2 telescope (UT2) at ESO's VLT on September 18, 2018 (a week after perihelion, $r_h = 1.01$ au and $\Delta = 0.40$ au) under Director's Discretionary Time. We used the UVES standard settings DIC#1 346+580 covering the range 3030 to 3880 Å in the blue and 4760 to 6840 Å in the red. We used a 0.44″ wide slit, providing a resolving power $R \sim 80\,000$. We obtained one single exposure of 3000 s at 8h35 UT with a mean air-mass of 1.7. This exposure provided two different spectra, which covered one of the above mentioned spectral ranges each.

The ESO UVES pipeline was used to reduce the spectra in the extended-object mode, keeping the spatial information. The spectra were corrected for the extinction and flux calibrated using the UVES master response curve provided by ESO.

[2] http://asteroid.lowell.edu/comet/dustphase.html

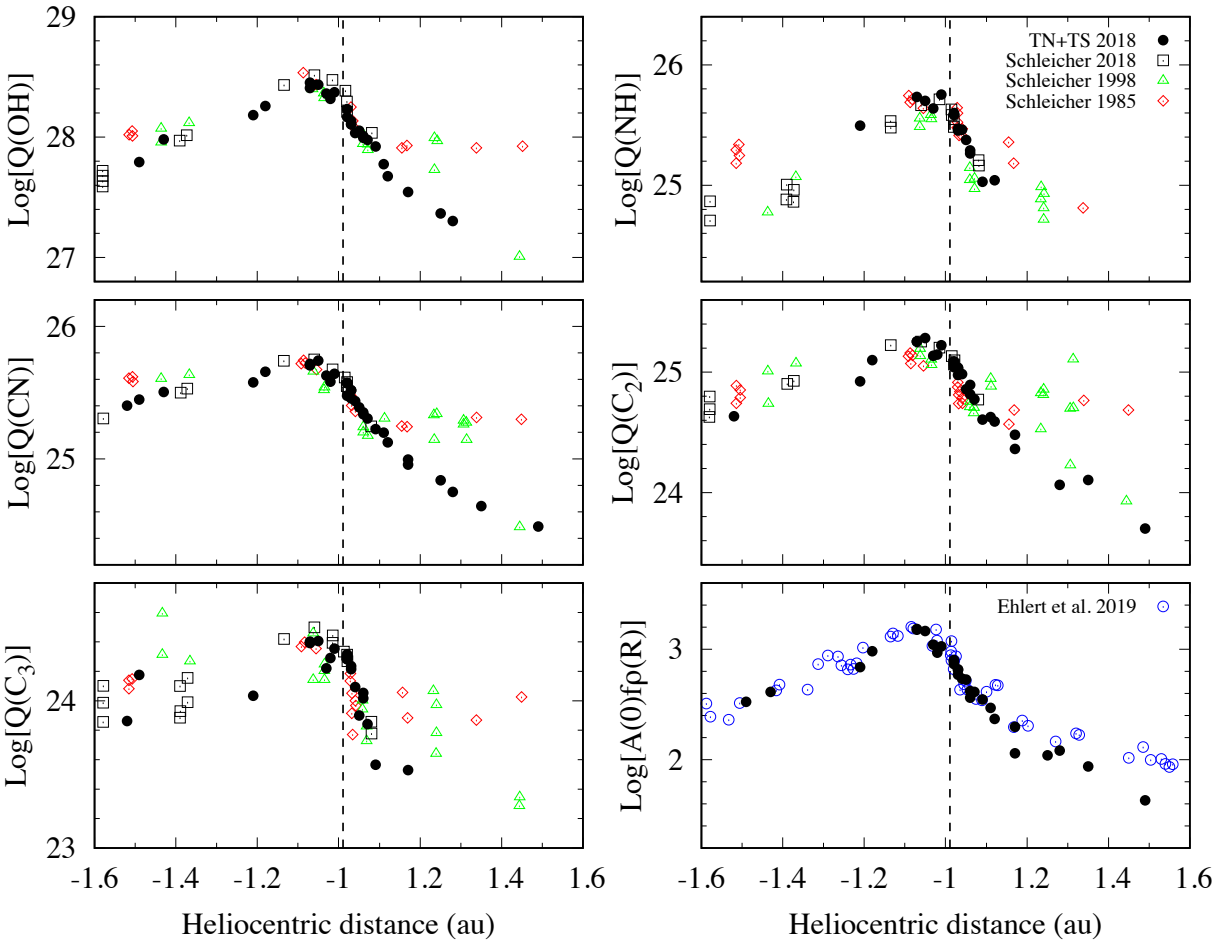

Fig. 1. Logarithm of the production rates (in mol s^{-1}) of each observed species and of the $A(0)f\rho$ parameter (in cm) of comet 21P during its 2018 return (this work and Schleicher & Knight 2018) compared with two previous apparitions in 1985 and 1998 (Schleicher & Knight 2018) as a function of heliocentric distance. The dashed vertical line represents the perihelion distance on September 10, 2018. The maximum of the gas and dust activity was reached at 1.07 au from the Sun on August 17, 2018, 24 days before perihelion.

One-dimensional spectra were then extracted by averaging the 2D spectra with simultaneous cosmic-ray rejection and then corrected for the Doppler shift due to the velocity of the comet with respect to Earth. More details about the UVES data reduction are given in the UVES manual[3]. The dust-reflected sunlight was finally removed using a reference solar spectrum BASS2000[4]. A more detailed description of the steps for UVES data reduction and the solar spectrum subtraction is given in Manfroid et al. (2009) and references therein.

3. Activity and composition

3.1. Gas-production rates

Along with our monitoring of comet 21P with the TRAPPIST telescopes, we derived the OH, NH, CN, C_3, and C_2 production rates. They are summarised in Table A.2, and their evolution as a function of the heliocentric distance is compared with two previous passages in Fig. 1.

We started to detect most of the radicals in the coma by the end of June 2018 (except for NH, which was detected one month later). The various production rates and the dust activity slowly increased as the comet approached the Sun (from 1.52 to 1.07 au). The highest activity was reached at 1.07 au from the Sun, on August 17, 24 days before perihelion. It then started to decrease rapidly after perihelion. CN was detected in our data until the end of 2018 at 1.66 au, while OH, C_3, and C_2 were no longer detected after the beginning of November at 1.4 au and NH in early October at 1.2 au. We found that like for the previous apparitions (Schleicher et al. 1987), the production rates pre-perihelion are higher by more than a factor two than post-perihelion. It is clear from Fig. 1 that the asymmetric activity is seen for all species, and this behaviour does not change over the various apparitions (Schleicher et al. 1987; Combi et al. 2011), as shown also in Fig. 2 for the water-production rate. The same behaviour has been reported for the parent molecule (H_2O, CO, CH_4, C_2H_2, C_2H_6, NH_3, and CH_3OH) production rates derived at IR wavelengths during the 2018 passage (Faggi et al. 2019; Roth et al. 2020). This might be due to the shape of the nucleus and its spin-axis orientation. This effect has been observed in several comets, such as 9P/Tempel 1 (Schleicher 2007), 81P/Wild 2 (Farnham & Schleicher 2005), and also for comet 67P/Churyumov-Gerasimenko (Schleicher 2006; Opitom et al. 2017). It has been shown very clearly by the Rosetta mission that the highest activity of 67P was clearly associated with the illumination of the most southern regions, which received the highest solar flux, and were subject to intense erosion

[3] ftp://ftp.eso.org/pub/dfs/pipelines/uves/uves-pipeline-manual-22.17.pdf
[4] http://bass2000.obspm.fr/solar_spect.php

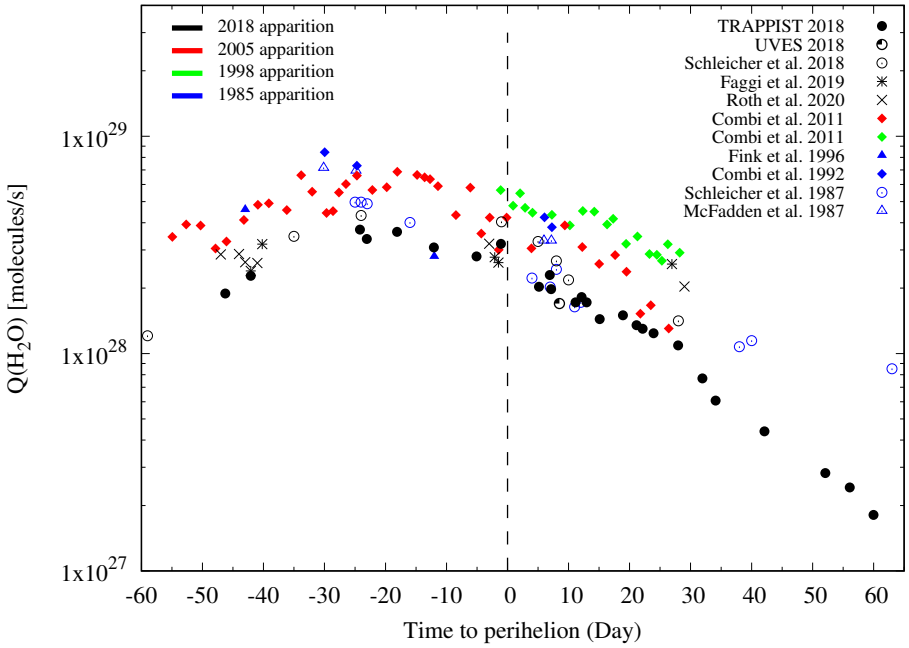

Fig. 2. H_2O production rates of comet 21P as a function of days to perihelion in 2018 compared to the previous apparitions (1985, 1998, and 2005). The data are described in more detail in Sect. 3.2.

(Lai et al. 2019). Recently, Marshall et al. (2019) have show for those three comets that the nucleus shape, the spin-axis orientation, and the distribution of activity on the cometary surface can explain the light curve of the water-production rate as a function of the heliocentric distance.

Around the activity maximum, the production rates are almost the same as those measured in the previous apparitions, showing that the activity level of 21P did not decrease over the last five orbits. Our production rates usually agree very well with those derived by Schleicher & Knight (2018), who used the same technique, while we note a discrepancy at large heliocentric distance and post-perihelion in the 1985 and 1998 apparition data (Schleicher et al. 1987; Schleicher & Knight 2018). This could be due to a sensitivity problem in their data as the production rates seem to level off on either side of perihelion, while the distance increased to a higher activity level of the comet after perihelion in the past. It has been also found that there is no significant change in the production rates of hypervolatile molecules (CO, CH_4, and C_2H_6) in comet 21P over the three different apparitions, 1998 (Weaver et al. 1999; Mumma et al. 2000), 2005 (DiSanti et al. 2012), and 2018 (Faggi et al. 2019; Roth et al. 2020).

3.2. H_2O production rate

The water-production rate is the most significant indicator of the activity of a comet. It can be measured directly from near-infrared observations or derived from OH emission at 3090 Å and radio wavelengths or from H Lyman-α emission at 1216 Å (Combi et al. 1986) assuming that both OH and H arise from the dissociation of H_2O. In this work, we computed the vector-equivalent water-production rates according to an empirical procedure based on a comparison of OH and water-production rates derived from the mean lifetimes, velocities, and scale lengths given by Cochran & Schleicher (1993). Schleicher et al. (1998) built an empirical relationship $Q(H_2O) = 1.361 r_h^{-0.5} Q(OH)$ based on an $r_h^{-0.5}$ dependence of the H_2O outflow velocity, a photodissociation branching ratio for water to OH of 90%, and the heliocentric distance. Figure 2 shows the water production we derived compared to previous apparitions (with different techniques) as a function of days to perihelion. We used the formula given above to convert Q(OH) into water production rates for the Schleicher & Knight (2018) data. Combi et al. (2011) derived the production rates from the H Ly-α emission observed by the Solar Wind ANisotropy (SWAN) instrument on board the Solar and Heliospheric Observatory (SOHO) in 1998 and in 2005. The Combi & Feldman (1992) values are derived from H Ly-α emission observed by the IUE mission for the 1985 apparition. From the Pioneer Venus Orbiter ultraviolet system (UVS) instrument, McFadden et al. (1987) derived the water-production rates from OH (3090 Å) emission. Fink & Hicks (1996) derived the water-production rates from the [OI](^{1}D) forbidden-line doublet using the correlation between the water-production rates and the total photon luminosity. Faggi et al. (2019) and Roth et al. (2020) measured the water-production rates directly from near-infrared spectra. TRAPPIST and UVES data points are from this work (see Sects. 3.2 and 5.1). The maximum in the last four apparitions was reached about one month before perihelion and does not change over all apparitions, but we observe a clear systematic difference between the narrow-band and spectroscopic methods in the optical on one hand and the measurements made from the space observations of the H Ly-α emission in the UV on the other hand. The maximum of the water production we measured was on August 17, 24 days before perihelion, and it reached $(3.72 \pm 0.07) \times 10^{28}$ mol s^{-1}, in good agreement with the Schleicher & Knight (2018) measurement of 4.20×10^{28} mol s^{-1} at the heliocentric distance of 1.07 au. Using the same technique for the 1985 apparition, Schleicher et al. (1987) reported $Q(H_2O) = 4.85 \times 10^{28}$ mol s^{-1} when the comet was at 1.05 au from the Sun. Using high-resolution infrared spectroscopy, Weaver et al. (1999) measured ~2–3 $\times 10^{28}$ mol s^{-1} at $r_h = 1.10$ au in 1998. For the 2005 apparition, Combi et al. (2011) found a value of 5.80×10^{28} mol s^{-1} from the H Ly-α emission observed by the SWAN/SOHO at $r_h = 1.08$ au. Comparing these data, we found that the water-production rates measured by Combi & Feldman (1992) in 1985 and Combi et al. (2011) in 2005 are systematically higher by a factor of about two than our results in

Table 2. Active area (km^2) and active fraction of the surface (%) for 21P using the slow-rotator model at some interesting heliocentric distances.

Date UT	r_h (au)	Active area (km^2)	Active fraction (%)
(a) 2018 Jun. 22	–1.49	4.9 ± 0.1	17.5 ± 11.6
(b) 2018 Aug. 17	–1.07	12.0 ± 0.2	42.5 ± 28.0
(c) 2018 Sep. 09	–1.01	9.0 ± 0.2	32.0 ± 21.3
(d) 2018 Sep. 15,16,17	+1.02	6.9 ± 0.1	21.5 ± 14.0
(e) 2018 Nov. 09	+1.31	0.90 ± 0.04	3.3 ± 2.2

Notes. (a) The first measurement during our monitoring campaign, (b) the maximum activity during our monitoring campaign, (c) the last measurement before perihelion passage, (d) the mean of the first measurements after perihelion passage with similar heliocentric distances of 1.02 au, and (e) the last and minimum measurements during our monitoring campaign. Large errors in the active fractions of the surface come from the large uncertainties in the radius of the nucleus, which we adopted as 1.5 ± 0.5 km (see Sect. 3.3 for details).

2018. This offset between various techniques has been reported in previous studies and as early as in studies for comet 1P/Halley (Schleicher et al. 1998). The origin of this discrepancy is not clear, but it is obvious that the agreement is good when the same technique is used. This indicates that the level of activity of 21P was the same over the past four decades and did not decrease, like that of comet 41P/Tuttle-Giacobini-Kresak, which lost as much as 30 to 40% of its activity from one orbit to the next (Moulane et al. 2018).

3.3. Active area of the nucleus

To estimate the active area of the nucleus surface, we modelled the water production using the sublimation model of Cowan & A'Hearn (1979). Because of the low thermal inertia of cometary nuclei (Gulkis et al. 2015), the slow-rotator approach was adopted in a number of cases as the most appropriate way for computing the cometary out-gassing (see e.g. Bodewits et al. 2014; Lis et al. 2019). The slow-rotator model assumes that every facet of the nucleus is in equilibrium with the solar radiation incident upon it, with the rotational pole pointed at the Sun. As mentioned previously, the size of the 21P nucleus, which is necessary to convert the active area into the active fraction of the whole surface, is not well constrained so far, with a radius ranging from 1 to 2 km. To estimate the active fraction of the surface, we therefore assumed a radius of 1.5 ± 0.5 km. Moreover, we assumed a bond albedo of 5 and a 100% infrared emissivity (see e.g. A'Hearn et al. 1989; McKay et al. 2018, 2019). We found that the active area of 21P during our monitoring campaign varied from ~5 km^2 at 1.49 au pre-perihelion, reached a maximum of ~12 km^2 at 1.07 au pre-perihelion, and decreased to ~1 km^2 at 1.31 au post-perihelion. Table 2 shows the lowest and highest active areas and active fraction for 21P using the slow-rotator model at some interesting heliocentric distances. We obtained different values than previous estimates given by Combi et al. (2019). The reason is twofold. First, the already mentioned discrepancy in the water-production rates found through different observational techniques (see Sect. 3.2), and second, the model used by the authors (fast rotator), which is less appropriate to describe the cometary outgassing.

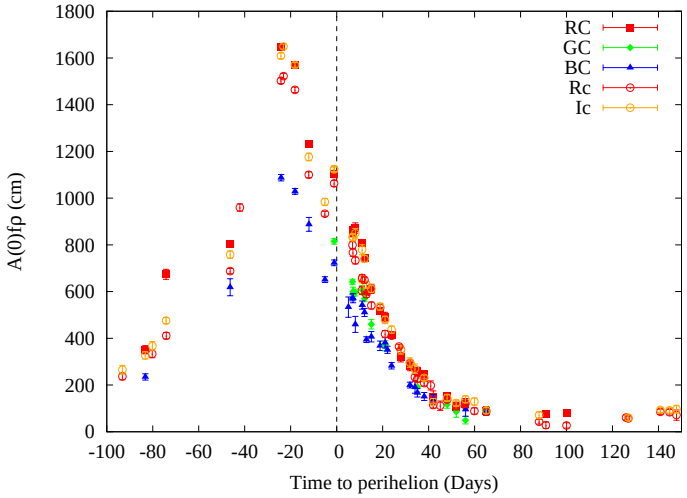

Fig. 3. $A(0)f\rho$ parameter measurements, computed at 10 000 km from the nucleus and corrected for the phase-angle effect, for the broad band (*Rc* and *Ic*) and narrow-band cometary filters (*RC*, *GC*, and *BC*) as a function of days to perihelion.

3.4. Dust properties

We computed the $A(0)f\rho$ parameter at 10 000 km, as defined by A'Hearn et al. (1984), using broad-band (*Rc* and *Ic*) and narrow-band dust continuum filters (*RC*, *GC*, *BC*) (see Table A.2). Figure 3 shows its evolution as a function of time to perihelion. Our results agree very well with those reported by Ehlert et al. (2019), as shown in the bottom right panel of Fig. 1. Like for the gas, the maximum was reached on August 17 with a value of (1646.1 ± 12.8) cm in the red narrow-band RC filter. About the same value was reported on previous apparitions at the same heliocentric distance (Schleicher et al. 1987; Lara et al. 2003; Pittichová et al. 2008). For a detailed description of the dust environment and its evolution, a more sophisticated model should be used, such as the Monte Carlo model presented by Moreno et al. (2012), which was used successfully in a number of cases (see e.g. Pozuelos et al. 2015, 2018; Moreno et al. 2016a,b, 2017). This study will be presented in a separate paper.

We used the $A(0)f\rho$ values obtained with the narrow-band filters, which are not contaminated by the gas emission, to derive the dust colours. The normalised reflectivity gradients between wavelength λ_1 and λ_2 are defined as (A'Hearn et al. 1984; Jewitt & Meech 1986)

$$S_v(\%/1000\,\text{Å}) = \frac{Af\rho_1 - Af\rho_2}{Af\rho_1 + Af\rho_2} \times \frac{2000}{\lambda_1 - \lambda_2}. \quad (1)$$

λ_1 and λ_2 are the effective wavelengths of the filters: *BC*[4450 Å], *GC*[5260 Å], and *RC*[7128 Å].

We found that the *RC*–*GC*, *RC*–*BC*, and *GC*–*BC* colours are redder than those of the Sun, with mean values of (14.8 ± 3.3), (13.2 ± 2.6), and (12.4 ± 7.5)%/1000 Å, respectively (see Fig. 4). This result agrees with previous apparitions, with values of $S_v = 15$%/1000 Å in 1985 (Schleicher et al. 1987) and $S_v = 13$%/1000 Å in 1998 (Lara et al. 2003). These values are consistent with the colour of the nucleus of 21P (12.8 ± 2.7)%/1000 Å measured at a heliocentric distance of 3.5 au in 1991 (Luu 1993). They fall within the range observed for most JFCs (Lamy & Toth 2009; Solontoi et al. 2012;

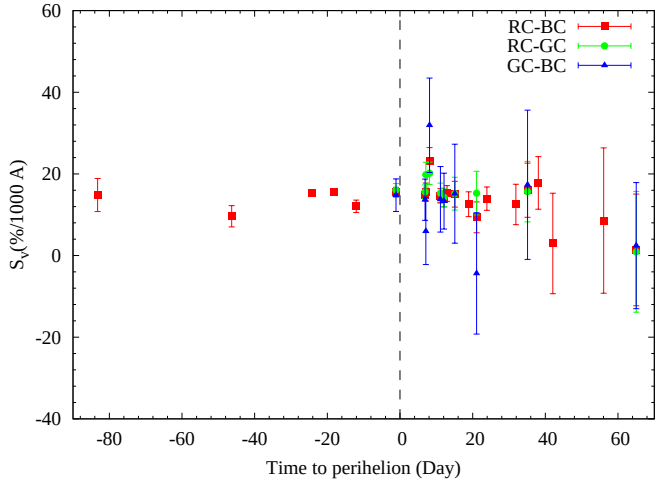

Fig. 4. Normalised reflectivity gradients S_v(% per 1000 Å) of comet 21P for different colour indices as a function of days to perihelion.

Jewitt 2015). During our long monitoring, we did not detect any significant variation in the colour of the dust in the coma (or any outburst).

4. Abundance ratios

The molecular abundances and their ratios with respect to the distance to the Sun give information about the homogeneity of a cometary nucleus and the chemical processes involved in the coma. Based on the relative abundance of 41 comets, A'Hearn et al. (1995) classified comets into two groups based on their C_2-to-CN ratio. Typical comets are defined as those having a $\log[Q(C_2)/Q(CN)] \geq -0.18$, while the carbon-chain-depleted comets are those below that value. This classification was confirmed later by other photometric and spectroscopic studies of large data sets (Schleicher 2008; Fink 2009; Langland-Shula & Smith 2011; Cochran et al. 2012) and must reflect some differences between the formation conditions (the pristine scenario) or a change of relative composition with time (several perihelion passages) of these comets (the evolutionary scenario). Figure 5 shows the evolution of the 21P abundance ratios of the various radicals with respect to OH (a proxy of water) and CN as a function of heliocentric distance. It is clear that the 21P abundance ratios in the 2018 return agree with the mean values of depleted comets given in A'Hearn et al. (1995). Table 3 summarises the relative abundances in 2018 compared to 1985 and 1998 data using the same technique and the same Haser model parameters (Schleicher & Knight 2018). Our 2018 ratios are the mean values for all the data obtained (see Table A.2). Like for the activity level over the past passages, the relative abundances did not change over the last five orbits. We note that the $Af\rho$ values derived in 1985 and in 1998 by Schleicher & Knight (2018) were computed for the narrow-band GC[5260 Å] filter, while we used the BC[4450 Å] filter. After correcting their $Af\rho$ values for the phase-angle effect using the same function as for the TRAPPIST data (see Sect. 2.1), the two data sets agree. This indicates that there is no evidence of changes in the chemical composition in the coma of the comet at different heliocentric distances (in the range 1.0 to 1.5 au) and over the five orbits, which is an argument for rejecting the evolutionary origin of the carbon-chain depletion in this comet.

The bottom panel of Fig. 5 shows that there is no evidence either that the dust-to-gas ratio represented by $A(0)f\rho/Q(CN)$ and $A(0)f\rho/Q(OH)$ depends on the heliocentric distance. We found that this ratio in 21P is consistent with the average value of depleted comets and higher than the mean value of the typical comets as defined in A'Hearn et al. (1995) (see Table 3). Lara et al. (2003) obtained a value of $\log[A(0)f\rho/Q(CN)] = -22.91 \pm 0.10$ in 1998 that agrees with our measurement. Like for the gas relative abundances, we conclude that the coma of 21P does not show significant variation in the dust-to-gas ratio over the previous apparitions and that it has a similar ratio as the depleted comets defined by A'Hearn et al. (1995).

Table 3. Relative molecular abundances of comet 21P over the last passages compared to the mean values for typical comets.

	Log production rate ratio			
	1985 [a]	1998 [a]	2018 [b]	Typical comets [c]
C_2/CN	–0.64	–0.50	-0.52 ± 0.10	0.06 ± 0.10
C_3/CN	–1.42	–1.30	-1.39 ± 0.12	-1.09 ± 0.11
CN/OH	–2.59	–2.67	-2.62 ± 0.08	-2.50 ± 0.18
C_2/OH	–3.23	–3.17	-3.16 ± 0.21	-2.44 ± 0.20
C_3/OH	–4.02	–3.98	-4.03 ± 0.16	-3.59 ± 0.29
NH/OH	–2.66	–2.87	-2.68 ± 0.14	-2.37 ± 0.27
$A(0)f\rho$/CN	–22.74	–22.73	-22.70 ± 0.04	-23.30 ± 0.32
$A(0)f\rho$/OH	–25.33	–25.42	-25.32 ± 0.04	-25.82 ± 0.40

References. [a] Schleicher & Knight (2018), [b] this work, [c] A'Hearn et al. (1995).

The comparison with abundances of parent molecules derived from IR data (Faggi et al. 2019; Roth et al. 2020) allows us to investigate the origin of the radicals observed in the atmosphere of 21P. Table 4 shows the comparison between the production rates of daughter molecules observed in the optical and the possible parent molecules observed at IR. Using high-resolution infrared spectra obtained in 1998, Weaver et al. (1999) reported upper limits for different species relative to H_2O such as C_2H_6 (2–3%), HCN(0.3–0.4%), and C_2H_2(0.5–0.8%) assuming that all species are parent molecules. C_2H_2 has been found to be depleted with respect to HCN by a factor five compared to other comets such as Hyakutake and Hale-Bopp. This result has been confirmed at this apparition by Faggi et al. (2019).

We derived a $Q(C_2) = 1.26 \times 10^{25}$ mol s^{-1}, which is consistent with the upper limit of $Q(C_2H_2) < 4.52 \times 10^{25}$ mol s^{-1} reported by Faggi et al. (2019) and $<1.80 \times 10^{25}$ mol s^{-1} reported by Roth et al. (2018) at 1.18 au from the Sun. This agreement indicates that C_2 might be a daughter species of C_2H_2. C_2 may also come from C_2H_6 and HC_2N (Helbert et al. 2005; Weiler 2012; Hölscher 2015) or be released from organic-rich grains (Combi & Fink 1997), but a detailed chemical model of the coma is required for more details. We also found a good match between $Q(CN) = 4.40 \times 10^{25}$ and $Q(HCN) = 4.30 \times 10^{25}$ mol s^{-1} (Faggi et al. 2019) at 1.01 au, showing that HCN might be the main parent molecule of CN in 21P. This result is known for several comets using different methods, including a comparison between the HCN and CN production rates (Rauer et al. 2003; Opitom et al. 2015b), coma morphology (Woodney et al. 2002), and also carbon and nitrogen isotopic ratios in both species (Manfroid et al. 2009; Bockelée-Morvan et al. 2015). We note, however, that in some cases, the two abundances do not agree, and other sources, for instance extended sources, have been claimed for the CN origin (Fray et al. 2005).

Some molecules such as C_4H_2, $CH_2C_2H_2$, and CH_3C_2H are proposed to be the parent molecules of C_3 (Helbert et al. 2005; Mumma & Charnley 2011; Hölscher 2015), but these complex

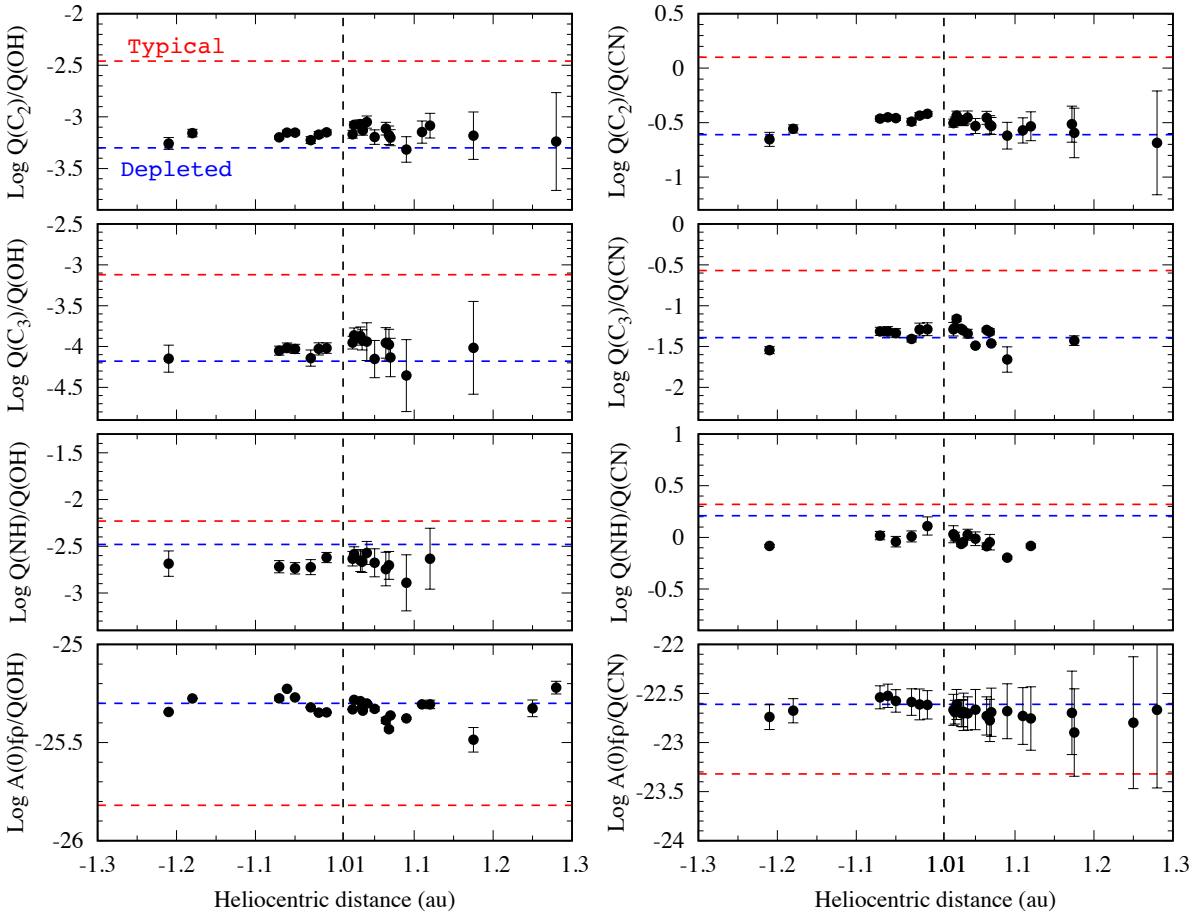

Fig. 5. Evolution of the logarithmic production rates ratios of each species with respect to OH and to CN as a function of heliocentric distance. The dashed red line represents the mean value of typical comets as defined in A'Hearn et al. (1995), while the blue line represents the mean value of the depleted group. *Bottom panels*: dust-to-gas ratio represented by $A(0)f\rho$-to-OH and $A(0)f\rho$-to-CN. The vertical dashed line shows the perihelion distance on September 10, 2018, at $r_h = 1.01$ au.

Table 4. Comparison of daughter molecules and possible parent molecule production rates derived from optical and infrared data of comet 21P in the 2018 passage.

UT date	r_h	Δ	Production rates (10^{25} mol s^{-1})									Reference
	(au)	(au)	Q(OH)	Q(H_2O)	Q(CN)	Q(HCN)	Q(C_2)	Q(C_2H_2)	Q(C_2H_6)	Q(NH)	Q(NH_3)	
2018 Jul 30	1.17	0.61	1810 ± 28		4.55 ± 0.07	–	1.26 ± 0.07	–	–	3.13 ± 0.50	–	This work
2018 Jul 30	1.17	0.61	–	2401 ± 394	–	<3.20	–	<4.52	4.49 ± 1.45	–	<63.72	Faggi et al. (2019)
2018 Jul 31	1.16	0.59	–	2503 ± 385	–	6.16 ± 0.12 [a]	–	<1.80 [a]	6.05 ± 0.77	–	<16.19 [a]	Roth et al. (2020)
2018 Sep 07	1.01	0.39	3036 ± 357	3206 ± 112	–	–	–	–	10.60 ± 1.10	–	–	Roth et al. (2020)
2018 Sep 09	1.01	0.39	–	2623 ± 586		4.30 ± 0.32		<0.62	8.30 ± 1.38		<12.59	Faggi et al. (2019)
2018 Sep 09	1.01	0.39	2360 ± 33		4.39 ± 0.07	–	1.67 ± 0.06	–	–	5.66 ± 0.38	–	This work
2018 Oct 07	1.07	0.49	–	2583 ± 864	–	–	–	–	4.55 ± 1.44	–	–	Faggi et al. (2019)
2018 Oct 08	1.08	0.49	834 ± 25	–	1.68 ± 0.05	–	0.40 ± 0.06	–	–	1.07 ± 0.35		This work
2018 Oct 10	1.10	0.51	–	2028 ± 255	–	–	–	–	2.92 ± 0.39	–	–	Roth et al. (2020)

Notes. [a]From Roth et al. (2018) measured on July 29, 2018. Upper limits are 3σ for the results of Roth et al. (2020) and Faggi et al. (2019).

species were not observed at infrared or at radio wavelengths. NH and NH_2 were found to be depleted in 21P in the previous apparitions (A'Hearn et al. 1995; Fink 2009). New infrared observations in 2018 show very low NH_3 in 21P, with an upper limit ratio of $Q(NH_3)/Q(H_2O) < 0.6\%$ (Faggi et al. 2019). In this work, we derive $Q(NH)/Q(OH) = 0.2\%$, which is consistent with $Q(NH_3)/Q(H_2O)$.

5. Optical high-resolution spectrum

5.1. Water-production rate

The UVES spectrum offered the possibility of independently computing the water-production rate at the time of observation. We first measured the overall flux for the OH (0,0) band near 309 nm, integrated over the whole slit. We found

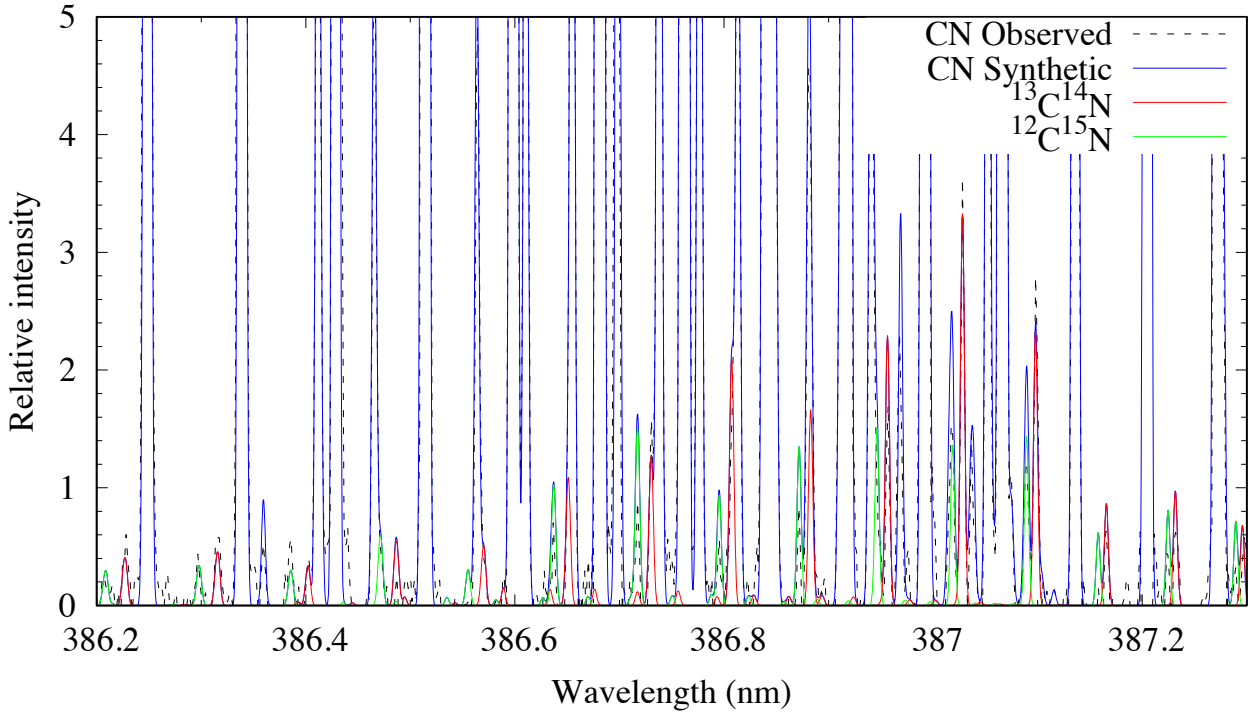

Fig. 6. Observed and synthetic CN spectra of the *R* branch of the B-X (0, 0) violet band in comet 21P.

1.47×10^{-13} erg s^{-1} cm^{-2} arcsec^{-2}. The fluorescence efficiency computed for this band and the heliocentric distance and velocity at the time of observation was 2.62×10^{-4} s^{-1} (or 1.71×10^{-15} erg s^{-1} mol^{-1} when scaled to 1 au; see details on the fluorescence model in Rousselot et al. 2019). From these values and a Monte Carlo simulation of the water molecules creating OH radicals in the inner coma (model based on equations given by Combi & Delsemme 1980) it is possible to compute the corresponding water-production rate for the number of OH radicals observed in the slit (0.44×9.5 arcsec) centred on the nucleus. Using the parameters of H_2O radial velocity, OH and H_2O lifetimes given in Cochran & Schleicher (1993) and assuming that 91.8% of water molecules dissociate to OH (Crovisier 1989), we found $Q(H_2O) = 1.7 \times 10^{28}$ mol s^{-1}. This result is in excellent agreement with the water-production rates computed from TRAPPIST observations in the same period (see Fig. 2). It must, nevertheless, be pointed out that it depends of the different parameters and can change slightly with them, especially with the water lifetime.

5.2. $^{12}C/^{13}C$ and $^{14}N/^{15}N$ isotopic ratios

The study of the isotopic ratios in comets has attracted considerable attention as it contains information about the conditions that prevailed at the time of formation of these objects in the early Solar System (Jehin et al. 2009; Hyodo et al. 2013). The carbon $^{12}C/^{13}C$ ratio has been determined for several comets from the analysis of the C_2 Swan band and CN B-X system in the optical (Manfroid et al. 2009; Bockelée-Morvan et al. 2015, and references therein). Some in situ measurements have also been obtained in comet 67P by the ROSINA mass spectrometer on board the Rosetta spacecraft for C_2H_4, C_2H_5, CO (Rubin et al. 2017), and CO_2 molecules (Hässig et al. 2017). All derived values are compatible with the terrestrial ratio of 89, except for CO, which might be slightly enriched in ^{13}C. The nitrogen $^{14}N/^{15}N$ isotopic ratio was measured for the first time from high-resolution spectra of the CN violet band in comets C/2000 WM1 (LINEAR) and C/1995 O1 (Hale-Bopp) and was found to be enriched by a factor of two in ^{15}N with respect to the Earth value (Arpigny 2003). The same ratio was found later from sub-millimeter observations of HCN in comet 17P/Holmes during its outburst and archival data of C/1995 O1 (Hale-Bopp) (Bockelée-Morvan et al. 2008). It has also been possible recently to measure the $^{14}N/^{15}N$ ratio in ammonia via the NH_2 radical (Rousselot et al. 2014). The values obtained are similar to the value found in HCN and CN, which was confirmed by subsequent works (Shinnaka et al. 2014, 2016; Rousselot et al. 2015; Shinnaka & Kawakita 2016; Yang et al. 2018). Recent measurements performed by the ROSINA mass spectrometer in comet 67P provided a ratio $^{14}N/^{15}N = 118 \pm 25$ for NH_3 and 130 ± 30 for N_2 molecules (Altwegg et al. 2019).

We used the $^{12}C^{14}N$ B-X (0,0) band to estimate the $^{12}C/^{13}C$ and $^{14}N/^{15}N$ isotopic ratios of 21P. We used a CN fluorescence model to create synthetic spectra of $^{13}C^{14}N$, $^{12}C^{15}N$, and $^{12}C^{14}N$. More details of the model are given in Manfroid et al. (2009). Figure 6 shows the observed CN spectrum compared to the synthetic spectrum made under the same observational conditions. The ratios found for $^{12}C/^{13}C$ and $^{14}N/^{15}N$ are 100 ± 10 and 145 ± 10, respectively. These values are consistent with those of about 20 comets with different dynamical origins, 91.0 ± 3.6 and 147.8 ± 5.7 for $^{12}C/^{13}C$ and $^{14}N/^{15}N$, respectively (Manfroid et al. 2009; Bockelée-Morvan et al. 2015).

5.3. NH_2 and NH_3 ortho-to-para ratios

We measured the ortho-to-para abundance ratio (OPR) of NH_2 from the three rovibronic emissions bands (0,7,0), (0,8,0), and (0,9,0), see Fig. 7, following the method described in Shinnaka et al. (2011). The derived OPRs of NH_2 and of its parent molecule NH_3 are listed for each band in Table 5, and they have

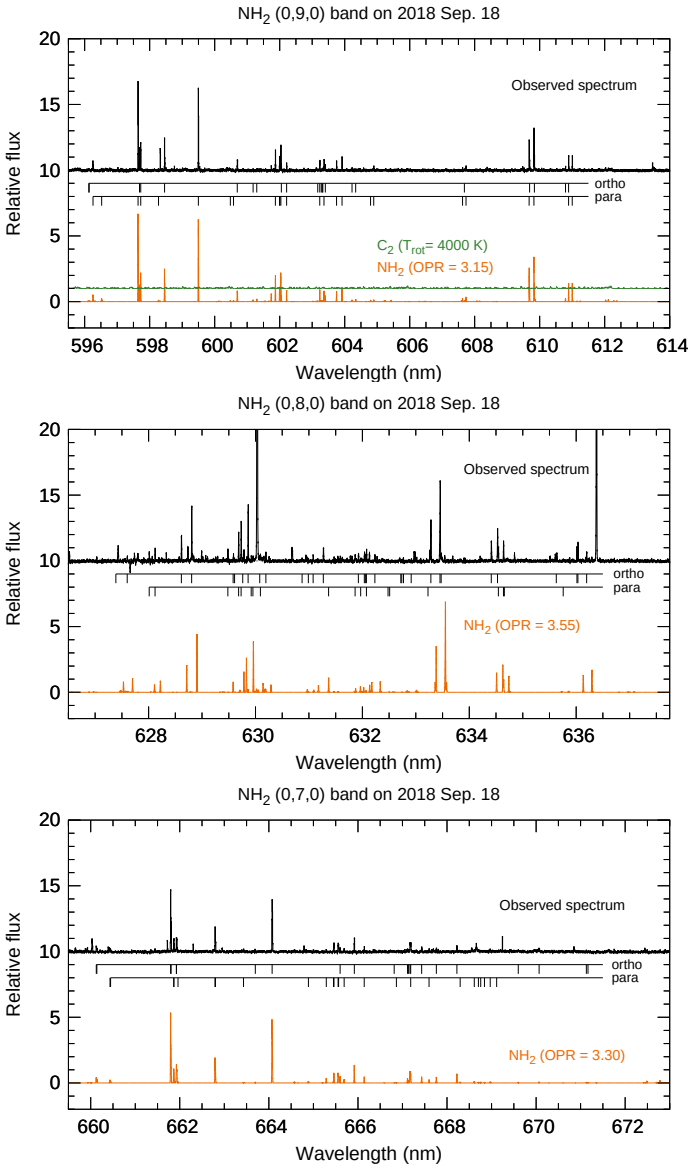

Fig. 7. Comparison between the observed and modelled spectra of the NH_2(0,9,0), (0,8,0), and (0,7,0) bands. The modelled spectrum of C_2 is also plotted in the NH_2 (0,9,0) band panel, but because of the depleted nature of 21P, the C_2 lines do not affect the NH_2 spectrum. The ortho- and para-lines of NH_2 are labelled in these modelled spectra. The two strong emission lines at 6300 and 6364 Å are the forbidden oxygen lines in the NH_2 (0,8,0) band panel. We note that the intensity ratio among bands is not correct because we scaled intensity for each plot independently.

average values of 3.38 ± 0.06 and 1.19 ± 0.03, respectively. The latter is in very good agreement with the Subaru/HDS determination (NH_3 OPR = 1.16 ± 0.02; Shinnaka et al. 2020). A nuclear spin temperature (T_{spin}) for ammonia of 27 ± 1 K was derived. The 21P value is consistent with typical values measured in comets (see Fig. 8). 21P therefore cannot be distinguished from other comets based on its NH_2 OPR (see Fig. 9), which is a possible cosmogonic indicator linked to the formation temperature of the molecule.

We would like to point out that recent laboratory experiments demonstrate that the OPR of water does not retain the memory of its formation temperature (Hama et al. 2011, 2016; Hama & Watanabe 2013). It is likely that this is also the case for ammonia.

Table 5. Derived NH_2 and NH_3 OPRs in comet 21P.

NH_2 band	NH_2 OPR	NH_3 OPR	T_{spin} (K)
(0,7,0)	3.30 ± 0.13	1.15 ± 0.07	$28^{+5}/_{-3}$
(0,8,0)	3.55 ± 0.08	1.28 ± 0.04	$23^{+2}/_{-1}$
(0,9,0)	3.15 ± 0.10	1.08 ± 0.05	$34^{+8}/_{-4}$
Average	3.38 ± 0.06	1.19 ± 0.03	27 ± 1

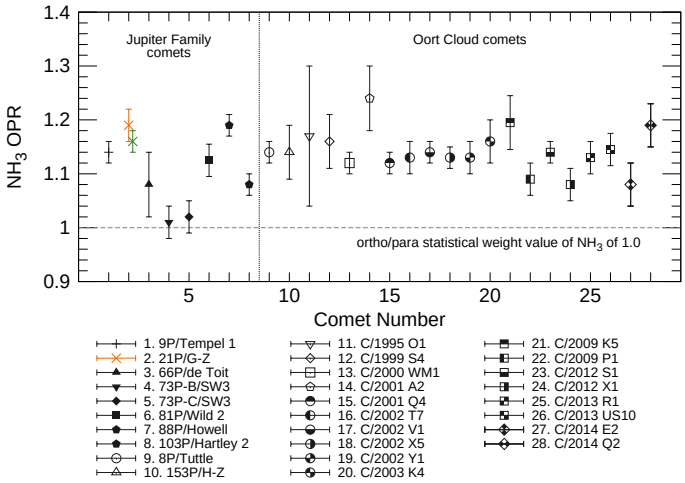

Fig. 8. Summary of NH_3 OPRs in comets. The orange and green crosses are the NH_3 OPR of 21P by VLT/UVES (this work) and by Subaru/HDS (Shinnaka et al. 2020), respectively.

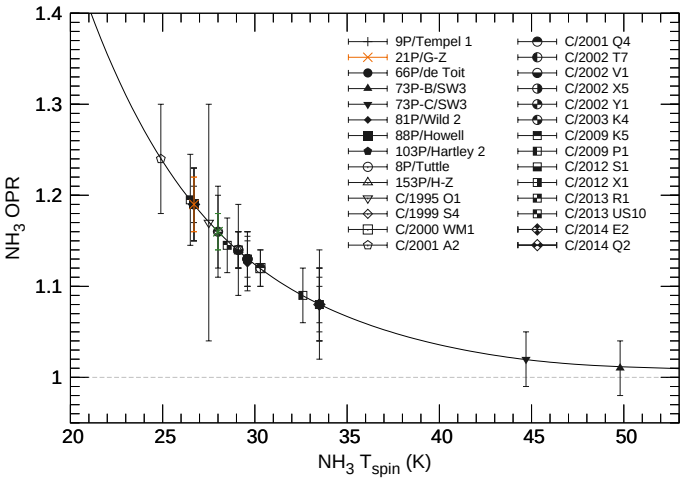

Fig. 9. Summary of the NH_3 T_{spin} in 28 comets of various origins. The orange and green crosses are the NH_3 T_{spin} of 21P by VLT/UVES (this work) and by Subaru/HDS (Shinnaka et al. 2020), respectively.

The OPRs of cometary volatiles might have been modified by an ortho-to-para conversion process in the inner coma or other catalyst activities of dust crust surfaces of the nucleus rather than be reflected by a formation temperature in the solar nebula 4.6 Gyr ago. OPRs might be a diagnostic of the physico-chemical conditions in the innermost coma or beneath the surface.

6. Dynamical evolution

In this section we analyse the dynamical evolution of the comet within the last 10^5 yr. JFCs are highly chaotic objects, whose

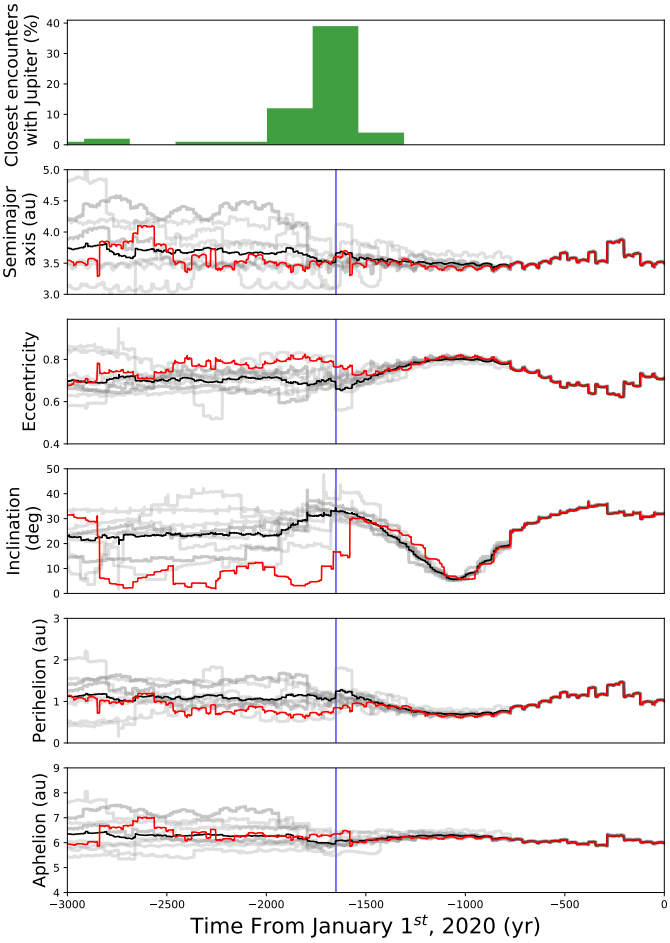

Fig. 10. Orbital evolution of 21P and its 200 clones for 3000 yr backward in time from January 1, 2020. *From top to the bottom*: closest approaches with Jupiter, semi-major axis, eccentricity, inclination, perihelion, and aphelion distance. In all panels, the grey lines correspond to the evolution of each clone, the black line is the mean value of the clones, and the red line is that of the nominal comet 21P. The vertical blue line corresponds to the time of the closest encounter with Jupiter. The initial orbital elements were taken from the JPL Small-Body Data Browser (orbital solution JPL K182/3).

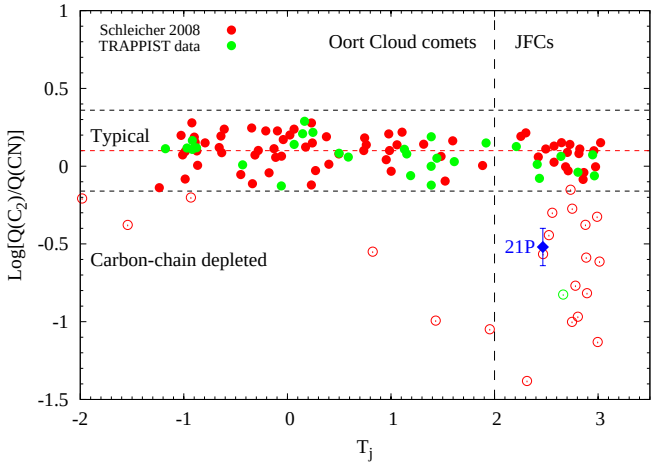

Fig. 11. Logarithm of C_2-to-CN ratio of 110 comets as a function of the Tisserand invariant parameter with respect to Jupiter (T_J). Filled symbols present typical comets, while the open symbols present the carbon-chain-depleted comets. Our measurement of comet 21P is represented by a blue diamond. The vertical dashed line at $T_j = 2$ separates the families of JFCs and Oort cloud comets.

dynamic evolution must be studied in terms of statistics (Levison & Duncan 1994). With this in mind, we analysed the evolution of the original object, that is, comet 21P, by considering the nominal values of its orbital parameters as they are defined in JPL-HORIZONS (orbital solution JPL K182/3). In the analysis, 200 clones were generated following the covariance matrix of its orbital parameters[5]. We performed the integration with the numerical package MERCURY (Chambers 1999), using the integration algorithm of Bulirsch-Stoer (Bulirsch & Stoer 1964) with a time step of 8 d, and we included the Sun, all planets, and Pluto in the simulation. In addition, we also included non-gravitational forces. The results of the simulations are displayed in Fig. 10.

We find that the orbits of all the clones in the simulation were very compact for a period of ~1650 yr. After that period, the orbits started to scatter, which was provoked by a close encounter with Jupiter, at a mean distance of 0.1 au. Because the nature of JFCs is chaotic, a comparison of results from different authors who applied different methods (e.g. different integration algorithm, different number of clones, or different manner in which their clones were generated) is difficult to perform, and any superficial comparison might yield incorrect conclusions. Only one analysis identical to that performed here has been carried out for comet 66P/du Toit by Yang et al. (2019). The authors found that the comet belongs to the Jupiter family for at least $\sim 60 \times 10^3$ yr, and the stable nature of its orbit was evident. This result indicates that 21P likely is a young member of the Jupiter family that has crossed its perihelion ~230 times with similar distances of $q \sim 1.013$ au. The youth of 21P could explain its unusual composition. However, the lack of a statistic sample prevents us from robustly confirming this hypothesis.

7. Discussion

As mentioned above, C_2 and C_3 have been found to be depleted compared to CN in 21P more than 50 yr ago (Mianes et al. 1960; Herbig 1976; Schleicher et al. 1987). In the data set of A'Hearn et al. (1995), 21P was classified as the prototype of the group that is depleted in carbon-chain molecules. Figure 11 shows our C_2-to-CN ratio compared to 120 comets (90 comets from Schleicher 2008 and 30 comets from TRAPPIST database Opitom 2016) as a function of the Tisserand invariant parameter with respect to Jupiter (T_J). About 30% of the comets analysed were found to be depleted in carbon-chain elements by varying amounts, including different dynamical types of comets, two-thirds are JFCs, and one-third are LPCs (A'Hearn et al. 1995; Schleicher 2008; Fink 2009; Cochran et al. 2012). 21P was found to be also depleted in NH with respect to OH (A'Hearn et al. 1995). This result was confirmed by its depletion in NH_2 using spectro-photometric observations by Konno & Wyckoff (1989) in the 1985 apparition and later by Fink & Hicks (1996) in the 1998 passage. This depletion in both NH and NH_2 indicates that 21P is likely depleted in the parent molecule NH_3, which was recently confirmed by Faggi et al. (2019). 21P is not a unique case of a comet depleted in both carbon-chain and ammonia daughter species. A few others have been found, but with a lesser degree of depletion, such

[5] Both sets of the orbital parameters and the covariance matrix of the orbit for 21P are published together in the NASA/JPL small-body browser: https://ssd.jpl.nasa.gov/sbdb.cgi?sstr=21P;old=0;orb=0;cov=1;log=0;cad=0#elem

as 43P/Wolf-Harrington and the split comet 73P/Schwassmann-Wachmann 3 (A'Hearn et al. 1995; Fink 2009; Cochran et al. 2012). This indicates that there might be a small group of similar comets that formed under similar conditions and is different from other comets. According to taxonomy studies, however, no clear grouping associated with an abundance in NH has been identified.

Our long monitoring of the abundance ratios combined with previous studies (Schleicher & Knight 2018; Combi et al. 2011) rules out the evolutionary scenario (peculiar composition due to repeated passages to perihelion). Our observations show remarkably constant abundance ratios of the different species, especially the depleted C_2 and NH, before and after perihelion, and over months. The fact that these ratios are still the same after five orbits is in favour of a pristine composition rather than compositional changes due to repeated passages of the comet at perihelion.

It was argued that this peculiar composition might be linked to a higher formation temperature, closer to that of the Sun (Schleicher et al. 1987), or in a local disc around Jupiter, as was proposed for comet 73P (Shinnaka et al. 2011). We obtained high-resolution optical spectra with high S/N in order to investigate the C and the N isotopic ratios, as well as the NH_2 OPR. 21P appears to have a normal $^{14}N/^{15}N$ ratio and a normal NH_3 OPR, similar to other comets. This is in contrast with comet 73P, which has both peculiar $^{14}N/^{15}N$ and OPR (see Fig. 9 and Shinnaka et al. 2011). The two comets therefore are apparently not related, and the peculiar composition of 21P still needs to be explained. These peculiarities are clearly linked to the ice composition of the nucleus because the IR studies of the mother molecules also show the same kind of depletion, with an obvious link to the daughter species.

8. Summary and conclusion

We performed an extensive monitoring of comet 21P on either side of perihelion with TRAPPIST. The gas species production rates as well as the dust proxy, $A(0)f\rho$ parameter, were computed until the detection limit. We derived the water-production rates for this apparition, and we compared it, as well as the various abundance ratios, to previous passages. Using a sublimation model for the nucleus and the water-production rates, we constrained the active area of the nucleus surface using the slow-rotator approach. An accurate determination of the 21P nucleus parameters is needed to better constrain the active area fraction. Comet 21P shows an asymmetric activity with respect to perihelion, which might be due to the nucleus shape, the spin axis orientation, and the distribution of activity on the cometary surface. The maximum of the gas and dust activity was about 24 days before perihelion, similar to the previous apparitions. According to the molecular abundance relative to CN and OH, we confirm that 21P is depleted in C_2, C_3, and NH with respect to CN and to OH. A very good agreement between the abundance of the potential mother molecules measured in the IR (HCN, C_2H_2, and NH_3) and the daughter species from our optical observations has been found. We obtained a high-resolution UVES spectrum of 21P a week after perihelion, and we derived $^{12}C/^{13}C$ and $^{14}N/^{15}N$ isotopic ratios of 100 ± 10 and 145 ± 10 from the CN R-branch of the B-X (0, 0) violet band. The ammonia OPR was found to be equal to 1.19 ± 0.03, corresponding to a spin temperature of 27 ± 1 K. All these values agree with those found for several comets of different dynamical types and origins and do not show any peculiarity that could be related to the low-carbon-chain species and ammonia abundances. Our observations favour a pristine origin for this composition, rather than heterogeneity or evolutionary scenarios of the surface composition.

Acknowledgments. The research leading to these results has received funding from the ARC grant for Concerted Research Actions, financed by the Wallonia-Brussels Federation. TRAPPIST-South is a project funded by the Belgian Fonds (National) de la Recherche Scientifique (F.R.S.-FNRS) under grant FRFC 2.5.594.09.F. TRAPPIST-North is a project funded by the University of Liège, and performed in collaboration with Cadi Ayyad University of Marrakesh. E.J. and D.H. are FNRS Senior Research Associates. J.M. is Honorary Research Director of the FNRS. We thank NASA, David Schleicher and the Lowell Observatory for the loan of a set of HB comet filters. UVES observations made with ESO Telescopes at the La Silla Paranal Observatory under program DDT proposal 2101.C-5051.

References

A'Hearn, M. F., Schleicher, D. G., Millis, R. L., Feldman, P. D., & Thompson, D. T. 1984, AJ, 89, 579
A'Hearn, M. F., Campins, H., Schleicher, D. G., & Millis, R. L. 1989, ApJ, 347, 1155
A'Hearn, M. F., Millis, R. C., Schleicher, D. O., Osip, D. J., & Birch, P. V. 1995, Icarus, 118, 223
Altwegg, K., Balsiger, H., & Fuselier, S. A. 2019, ARA&A, 57, 113
Arpigny, C. 2003, Science, 301, 1522
Beaver, J. E., Wagner, R. M., Schleicher, D. G., & Lutz, B. L. 1990, ApJ, 360, 696
Beech, M. 1986, AJ, 91, 159
Bessell, M. S. 1990, PASP, 102, 1181
Bockelée-Morvan, D., Biver, N., Jehin, E., et al. 2008, ApJ, 679, L49
Bockelée-Morvan, D., Calmonte, U., Charnley, S., et al. 2015, Space Sci. Rev., 197, 47
Bodewits, D., Farnham, T. L., A'Hearn, M. F., et al. 2014, ApJ, 786, 48
Bulirsch, R., & Stoer, J. 1964, Numer. Math., 6, 413
Chambers, J. E. 1999, MNRAS, 304, 793
Cochran, A. L., & Barker, E. S. 1987, AJ, 93, 239
Cochran, A. L., & Schleicher, D. G. 1993, Icarus, 105, 235
Cochran, A., Barker, E., & Gray, C. 2012, Icarus, 218, 144
Combi, M. R., & Delsemme, A. H. 1980, ApJ, 237, 633
Combi, M. R., & Feldman, P. D. 1992, Icarus, 97, 260
Combi, M. R., & Fink, U. 1997, ApJ, 484, 879
Combi, M. R., Stewart, A. I. F., & Smyth, W. H. 1986, Geophys. Res. Lett., 13, 385
Combi, M. R., Bertaux, J.-L., Quémerais, E., Ferron, S., & Mäkinen, J. T. T. 2011, ApJ, 734, L6
Combi, M. R., Mäkinen, T. T., Bertaux, J. L., Quémerais, E., & Ferron, S. 2019, Icarus, 317, 610
Cowan, J. J., & A'Hearn, M. F. 1979, Moon Planets, 21, 155
Crovisier, J. 1989, A&A, 213, 459
DiSanti, M. A., Bonev, B. P., Villanueva, G. L., & Mumma, M. J. 2012, ApJ, 763, 1
Egal, A., Wiegert, P., Brown, P. G., et al. 2019, Icarus, 330, 123
Ehlert, S., Moticska, N., & Egal, A. 2019, AJ, 158, 7
Faggi, S., Mumma, M. J., Villanueva, G. L., Paganini, L., & Lippi, M. 2019, AJ, 158, 254
Farnham, T., & Schleicher, D. 2005, Icarus, 173, 533
Farnham, T. L., Schleicher, D. G., & A'Hearn, M. F. 2000, Icarus, 147, 180
Fink, U. 2009, Icarus, 201, 311
Fink, U., & Hicks, M. D. 1996, ApJ, 459, 729
Fray, N., Bénilan, Y., Cottin, H., Gazeau, M.-C., & Crovisier, J. 2005, Planet. Space Sci., 53, 1243
Gulkis, S., Allen, M., von Allmen, P., et al. 2015, Science, 347, aaa0709
Hama, T., & Watanabe, N. 2013, Chem. Rev., 113, 8783
Hama, T., Watanabe, N., Kouchi, A., & Yokoyama, M. 2011, ApJ, 738, L15
Hama, T., Kouchi, A., & Watanabe, N. 2016, Science, 351, 65
Hanner, M., Veeder, G., & Tokunaga, A. 1992, AJ, 104, 386
Haser, L. 1957, Bull. Soc. R. Sci. Liege, 43, 740
Hässig, M., Altwegg, K., Balsiger, H., et al. 2017, A&A, 605, A50
Helbert, J., Rauer, H., Boice, D. C., & Huebner, W. F. 2005, A&A, 442, 1107
Herbig, G. H. 1976, Rev. of cometary spectra, 393, 136
Hölscher, A. 2015, PhD thesis, Technische Universität, Berlin
Hyodo, F., Kusaka, S., Wardle, D. A., & Nilsson, M.-C. 2013, Plant Soil, 364, 315
Jehin, E., Manfroid, J., Hutsemékers, D., Arpigny, C., & Zucconi, J.-M. 2009, Earth Moon Planets, 105, 167

Jehin, E., Gillon, M., Queloz, D., et al. 2011, The Messenger, 145, 2
Jewitt, D. 2015, AJ, 150, 201
Jewitt, D., & Meech, K. J. 1986, ApJ, 310, 937
Kiselev, N. N., Jockers, K., Rosenbush, V. K., et al. 2000, Planet. Space Sci., 48, 1005
Konno, I., & Wyckoff, S. 1989, Adv. Space Res., 9, 163
Królikowska, M., Sitarski, G., & Szutowicz, S. 2001, A&A, 368, 676
Lai, I.-L., Ip, W.-H., Lee, J.-C., et al. 2019, A&A, 630, A17
Lamy, P., & Toth, I. 2009, Icarus, 201, 674
Langland-Shula, L. E., & Smith, G. H. 2011, Icarus, 213, 280
Lara, L.-M., Licandro, J., Oscoz, A., & Motta, V. 2003, A&A, 399, 763
Leibowitz, E. M., & Brosch, N. 1986, Icarus, 68, 430
Levison, H. F., & Duncan, M. J. 1994, Icarus, 108, 18
Lis, D. C., Bockelée-Morvan, D., Güsten, R., et al. 2019, A&A, 625, L5
Luu, J. X. 1993, Icarus, 104, 138
Manfroid, J., Jehin, E., Hutsemékers, D., et al. 2009, A&A, 503, 613
Marshall, D., Rezac, L., Hartogh, P., Zhao, Y., & Attree, N. 2019, A&A, 623, A120
McFadden, L. A., A'Hearn, M. F., Feldman, P. D., et al. 1987, Icarus, 69, 329
McKay, A. J., Cochran, A. L., DiSanti, M. A., et al. 2018, Icarus, 309, 1
McKay, A. J., DiSanti, M. A., Kelley, M. S. P., et al. 2019, AJ, 158, 128
Mianes, P., Grudzinska, S., & Stawikowski, A. 1960, Ann. Astrophys., 23, 788
Moreno, F., Pozuelos, F., Aceituno, F., et al. 2012, ApJ, 752, 136
Moreno, F., Licandro, J., Cabrera-Lavers, A., & Pozuelos, F. J. 2016a, ApJ, 826, 137
Moreno, F., Licandro, J., Cabrera-Lavers, A., & Pozuelos, F. J. 2016b, ApJ, 826, L22
Moreno, F., Pozuelos, F. J., Novaković, B., et al. 2017, ApJ, 837, L3
Moulane, Y., Jehin, E., Opitom, C., et al. 2018, A&A, 619, A156
Mumma, M. J., & Charnley, S. B. 2011, ARA&A, 49, 471
Mumma, M. J., DiSanti, M. A., Russo, N. D., Magee-Sauer, K., & Rettig, T. W. 2000, ApJ, 531, L155
Opitom, C. 2016, Monitoring of the chemical composition of comets in the framework of the TRAPPIST survey, PhD thesis, Université de Liège, Liège, Belgium
Opitom, C., Jehin, E., Manfroid, J., et al. 2015a, A&A, 574, A38
Opitom, C., Jehin, E., Manfroid, J., et al. 2015b, A&A, 584, A121
Opitom, C., Snodgrass, C., Fitzsimmons, A., et al. 2017, MNRAS, 469, S222
Pittichová, J., Woodward, C. E., Kelley, M. S., & Reach, W. T. 2008, AJ, 136, 1127
Pozuelos, F. J., Cabrera-Lavers, A., Licandro, J., & Moreno, F. 2015, ApJ, 806, 102
Pozuelos, F. J., Jehin, E., Moulane, Y., et al. 2018, A&A, 615, A154
Rauer, H., Helbert, J., Arpigny, C., et al. 2003, A&A, 397, 1109
Roth, N., Gibb, E., Dello Russo, N., et al. 2018, AAS/Division for Planetary Sciences Meeting Abstracts, 50, 210.11
Roth, N. X., Gibb, E. L., Bonev, B. P., et al. 2020, AJ, 159, 42
Rousselot, P., Pirali, O., Jehin, E., et al. 2014, ApJ, 780, L17
Rousselot, P., Decock, A., Korsun, P. P., et al. 2015, A&A, 580, A3
Rousselot, P., Opitom, C., Jehin, E., et al. 2019, A&A, 628, A22
Rubin, M., Altwegg, K., Balsiger, H., et al. 2017, A&A, 601, A123
Scarf, F. L., Coroniti, F. V., Kennel, C. F., et al. 1986, Science, 232, 377
Schleicher, D. G. 2006, Icarus, 181, 442
Schleicher, D. 2007, Icarus, 190, 406
Schleicher, D. G. 2008, AJ, 136, 2204
Schleicher, D., & Knight, M. 2018, AAS/Division for Planetary Sciences Meeting Abstracts, 210.12
Schleicher, D. G., Millis, R. L., & Birch, P. V. 1987, A&A, 187, 531
Schleicher, D. G., Millis, R. L., & Birch, P. V. 1998, Icarus, 132, 397
Shinnaka, Y., & Kawakita, H. 2016, AJ, 152, 145
Shinnaka, Y., Kawakita, H., Kobayashi, H., et al. 2011, ApJ, 729, 81
Shinnaka, Y., Kawakita, H., Kobayashi, H., Nagashima, M., & Boice, D. C. 2014, ApJ, 782, L16
Shinnaka, Y., Kawakita, H., Jehin, E., et al. 2016, MNRAS, 462, S195
Shinnaka, Y., Kawakita, H., & Tajitsu, A. 2020, AJ, 159, 203
Solontoi, M., Ivezić, Ž., Jurić, M., et al. 2012, Icarus, 218, 571
Tancredi, G., Fernández, J. A., Rickman, H., & Licandro, J. 2000, A&AS, 146, 73
Von Rosenvinge, T. T., Brandt, J. C., & Farquhar, R. W. 1986, Science, 232, 353
Weaver, H., Chin, G., Bockelee-Morvan, D., et al. 1999, Icarus, 142, 482
Weiler, M. 2012, A&A, 538, A149
Woodney, L., AHearn, M., Schleicher, D. G., et al. 2002, Icarus, 157, 193
Yang, B., Hutsemékers, D., Shinnaka, Y., et al. 2018, A&A, 609, L4
Yang, B., Jehin, E., Pozuelos, F. J., et al. 2019, A&A, 631, A168

Appendix A: Observational circumstances and production rates of comet 21P with TRAPPIST telescopes

Table A.1. Observational circumstances of comet 21P with TRAPPIST telescopes.

UT date	r_h	Δ	ΔT	PA	Gas filters					Dust filters					Telescope
	(au)	(au)	(Days)	(°)	OH	NH	CN	C_2	C_3	*BC*	*RC*	*GC*	*Rc*	*Ic*	TN/TS
2018 Jun. 09	1.61	1.07	–93.20	38.01									6	1	TN
2018 Jun. 19	1.52	0.94	–83.25	40.98	1		1	1	1	1	1		1	1	TN
2018 Jun. 22	1.49	0.90	–80.16	41.98	1	1	1	1	1	1	1		5	1	TN
2018 Jun. 28	1.44	0.88	–74.20	44.13	1	1	2	1	1	1	1		6	2	TN
2018 Jul. 09	1.34	0.78	–63.30	48.62			2	1			1		3	1	TN
2018 Jul. 26	1.21	0.65	–46.25	56.96	1	1	2	1	1	1	1		3	1	TN
2018 Jul. 30	1.18	0.62	–42.25	59.13	1		2	2					4		TN
2018 Aug. 17	1.07	0.48	–24.25	69.44	1	1	2	1	1	1	1		6	1	TN
2018 Aug. 18	1.07	0.49	–23.08	69.99	1		1	1	1				5	1	TN
2018 Aug. 23	1.04	0.45	–18.13	72.65	1	1	1	1	1	1	1		5	1	TN
2018 Aug. 29	1.03	0.42	–12.11	75.38	1	1	1	1	1	1	1		5	1	TN
2018 Sep. 05	1.01	0.39	–05.10	77.67	1		3	1	1	1			5	1	TN
2018 Sep. 09	1.01	0.39	–01.10	78.01	1	1	2	1	1	1	1	1	8	4	TN
2018 Sep. 15	1.01	0.39	+05.09	77.40	2	1	1	1	1	1	1		5	1	TS
2018 Sep. 17	1.01	0.40	+06.90	76.83	1	1	3	1	1	1	1	1	11	2	TN
2018 Sep. 17	1.01	0.40	+06.90	76.83	1	1	1	1	1	1	1	1	5	3	TS
2018 Sep. 18	1.01	0.40	+08.13	76.53			1	1	1	1	1	1	5	3	TS
2018 Sep. 20	1.02	0.40	+10.12	75.84	1	1	1	1	1	1	1	1	5	3	TS
2018 Sep. 21	1.02	0.41	+11.12	75.45	1		1	1		1	1		3	1	TN
2018 Sep. 21	1.02	0.41	+11.12	75.45	1	1	1	1	1	1	1	1	5	3	TS
2018 Sep. 22	1.02	0.41	+12.12	75.04	1	1	1	1	1	1	1	1	5	3	TS
2018 Sep. 23	1.02	0.41	+12.95	74.61									3	1	TN
2018 Sep. 25	1.03	0.42	+15.10	73.63	1	1	2	2	1	1	1	1	5	3	TS
2018 Sep. 29	1.04	0.44	+18.90	71.61	2	2	2	2	2	2	2		6	2	TN
2018 Oct. 01	1.05	0.45	+21.10	70.49	2	1	2	2	1	1	1	1	5	3	TS
2018 Oct. 02	1.06	0.46	+22.10	69.92	1	1	1	1	1	1					TS
2018 Oct. 04	1.07	0.47	+23.90	68.69	1	1	2	2	2	2	2		6	2	TN
2018 Oct. 07	1.08	0.49	+27.13	66.92			1	1					1		TS
2018 Oct. 08	1.08	0.49	+27.90	66.37	1	1	1	1	1	1	1		11	1	TN
2018 Oct. 12	1.10	0.51	+31.90	64.55	1	1	1	2	1	1	2		10	2	TN
2018 Oct. 14	1.12	0.53	+34.10	62.73	1	1	1	1	1	1	1	1	5	1	TS
2018 Oct. 15	1.12	0.54	+35.10	62.12						1	1	1	5		TS
2018 Oct. 18	1.14	0.56	+38.11	60.33	1	1	1	1	1	1	1		3	2	TS
2018 Oct. 18	1.14	0.56	+37.90	60.33			1	1					1		TN
2018 Oct. 21	1.16	0.58	+40.95	58.55			1	1					3		TN
2018 Oct. 22	1.17	0.59	+42.06	57.97	1	1	1	1	1	1	1		5	2	TS
2018 Oct. 25	1.19	0.61	+45.10	56.25									1	1	TS
2018 Oct. 28	1.21	0.63	+48.09	54.55			1	1		1	1	1	1	1	TS
2018 Nov. 01	1.24	0.66	+52.04	52.37	1	1	1	1	1	1	1	1	4	1	TS
2018 Nov. 05	1.27	0.68	+56.05	50.80	1		1	1		1	1	1	4	1	TS
2018 Nov. 09	1.31	0.71	+59.98	48.27	1		1	1		1	1	1	4	1	TS
2018 Nov. 14	1.35	0.74	+65.10	45.84	1		1	1		1	1	1	5	1	TS
2018 Nov. 30	1.49	0.85	+81.08	38.84			1	1		1	1		3	1	TS
2018 Dec. 07	1.55	0.90	+88.12	36.12			1			1			3	1	TS
2018 Dec. 10	1.58	0.92	+91.10	35.01			1			1			3	1	TS
2018 Dec. 19	1.66	0.98	+100.05	32.04			1			1	1		4	1	TS
2018 Dec. 29	1.75	1.06	+110.12	29.28			1						1	1	TS
2019 Jan. 14	1.90	1.20	+126.13	26.20									2		TS
2019 Jan. 15	1.91	1.21	+127.10	26.08									3	1	TS
2019 Jan. 29	2.04	1.37	+141.12	24.74									4	1	TS
2019 Feb. 02	2.08	1.42	+145.08	24.52									4	1	TS
2019 Feb. 04	2.10	1.44	+147.11	24.43									4	4	TS

Notes. r_h and Δ are the heliocentric and geocentric distances, ΔT is the time to perihelion in days, (−) for pre-perihelion and (+) for post-perihelion. PA is the solar phase angle.

Table A.2. OH, NH, CN, C_2, and C_3 production rates and $A(\theta=0)f\rho$ measurements for comet 21P with the TN and TS telescopes.

UT date	r_h	Production rates ($\times 10^{24}$ mol s^{-1})					$A(\theta=0)f\rho$					TN/TS
	(au)	OH	NH	CN	C_2	C_3	*BC*	*RC*	*GC*	*Rc*	*Ic*	
2018 Jun. 09	1.61	–	–	–	–	–	–	–	–	236.5 ± 14.0	265.5 ± 18.7	TN
2018 Jun. 19	1.52	–	–	25.20 ± 0.52	4.30 ± 0.65	–	234.8 ± 13.6	351.1 ± 17.5	–	–	326.9 ± 15.6	TN
2018 Jun. 22	1.49	6200 ± 253	–	28.00 ± 0.53	–	1.50 ± 0.20	–	–	–	333.6 ± 16.8	367.5 ± 18.4	TN
2018 Jun. 28	1.44	9560 ± 365	–	32.00 ± 0.64	–	–	–	673.7 ± 21.4	–	411.0 ± 13.7	475.7 ± 12.9	TN
2018 Jul. 26	1.21	15 200 ± 322	31.30 ± 4.90	37.80 ± 0.54	8.40 ± 0.66	1.08 ± 0.20	618.6 ± 36.4	801.5 ± 12.9	–	687.8 ± 11.5	758.2 ± 15.9	TN
2018 Jul. 30	1.18	18 100 ± 278	–	45.50 ± 0.63	12.60 ± 0.65	–	–	–	–	959.8 ± 15.8	–	TN
2018 Aug. 17	1.07	28 300 ± 558	54.10 ± 4.59	52.00 ± 0.65	17.90 ± 0.64	2.52 ± 0.19	1087.6 ± 13.7	1646.1 ± 12.7	–	1502.7 ± 12.1	1609.3 ± 12.7	TN
2018 Aug. 18	1.07	25 600 ± 276	–	50.80 ± 0.64	18.00 ± 0.62	2.47 ± 0.17	–	–	–	1522.1 ± 11.6	1648.9 ± 10.3	TN
2018 Aug. 23	1.04	27 300 ± 304	50.20 ± 3.60	55.20 ± 0.67	19.20 ± 0.64	2.55 ± 0.17	1028.9 ± 12.5	1570.7 ± 11.8	–	1463.7 ± 11.7	1570.2 ± 10.0	TN
2018 Aug. 29	1.03	23 000 ± 286	43.50 ± 4.07	42.50 ± 0.62	13.70 ± 0.62	1.66 ± 0.18	887.6 ± 29.6	1229.9 ± 12.5	–	1100.0 ± 12.7	1176.3 ± 16.1	TN
2018 Sep. 05	1.01	20 800 ± 312	–	38.20 ± 0.64	14.00 ± 0.63	1.95 ± 0.17	651.2 ± 12.4	–	–	933.1 ± 10.5	984.0 ± 14.8	TN
2018 Sep. 09	1.01	23 600 ± 328	56.60 ± 3.86	43.90 ± 0.68	16.70 ± 0.64	2.26 ± 0.17	723.3 ± 12.4	1103.1 ± 15.7	815.5 ± 12.4	1062.9 ± 12.7	1123.3 ± 12.1	TN
2018 Sep. 17	1.01	17 100 ± 300	39.80 ± 3.77	37.10 ± 0.66	11.60 ± 0.64	1.91 ± 0.18	574.6 ± 14.1	861.6 ± 12.4	642.0 ± 10.7	799.0 ± 15.1	833.7 ± 14.0	TN
2018 Sep. 17	1.01	14 700 ± 326	38.30 ± 3.84	37.60 ± 0.53	12.30 ± 0.63	2.02 ± 0.22	571.6 ± 19.6	851.4 ± 17.2	599.9 ± 19.2	767.0 ± 16.2	832.1 ± 14.8	TS
2018 Sep. 18	1.01	–	–	30.00 ± 0.52	11.00 ± 0.65	2.07 ± 0.28	459.5 ± 34.2	872.2 ± 22.2	595.9 ± 14.8	733.3 ± 14.8	849.6 ± 20.4	TS
2018 Sep. 21	1.02	–	–	–	–	–	–	–	–	604.7 ± 16.6	652.2 ± 14.9	TN
2018 Sep. 21	1.02	1280 ± 212	28.50 ± 3.79	33.00 ± 0.52	10.90 ± 0.63	1.72 ± 0.22	542.3 ± 17.4	808.3 ± 12.5	606.4 ± 19.9	658.3 ± 14.9	779.5 ± 21.4	TS
2018 Sep. 22	1.02	13 600 ± 216	29.40 ± 3.84	32.80 ± 0.51	10.80 ± 0.65	1.64 ± 0.23	510.9 ± 17.4	744.0 ± 15.0	569.2 ± 12.5	649.8 ± 12.5	740.3 ± 14.7	TS
2018 Sep. 23	1.02	12 800 ± 249	–	28.60 ± 0.61	9.48 ± 0.62	–	394.5 ± 12.5	596.1 ± 12.5	–	–	629.3 ± 15.2	TN
2018 Sep. 25	1.03	10 880 ± 216	29.00 ± 4.15	27.30 ± 0.54	9.62 ± 0.76	1.24 ± 0.31	406.8 ± 22.4	611.7 ± 19.9	460.0 ± 20.1	540.5 ± 14.8	611.6 ± 15.3	TS
2018 Sep. 29	1.04	11 300 ± 254	23.80 ± 4.11	24.50 ± 0.58	7.21 ± 0.67	0.79 ± 0.19	368.1 ± 20.4	517.1 ± 15.1		530.7 ± 17.8	535.4 ± 15.2	TN
2018 Oct. 01	1.05	10 220 ± 217	18.40 ± 3.68	22.40 ± 0.52	7.84 ± 0.64	1.13 ± 0.23	381.4 ± 23.2	490.7 ± 20.6	368.1 ± 21.9	418.3 ± 15.3	478.8 ± 15.7	TS
2018 Oct. 02	1.06	9860 ± 182	19.50 ± 3.27	21.70 ± 0.52	6.55 ± 0.71	1.04 ± 0.21	350.8 ± 15.3	–	–	–	–	TS
2018 Oct. 04	1.07	9460 ± 268		20.20 ± 0.55	5.95 ± 0.63	0.70 ± 0.18	282.6 ± 14.0	412.3 ± 12.2	–	411.2 ± 12.2	437.4 ± 15.4	TN
2018 Oct. 08	1.08	8340 ± 248	10.70 ± 3.53	16.80 ± 0.53	4.03 ± 0.61	0.36 ± 0.17	–	318.5 ± 19.9	–	350.5 ± 12.2	350.5 ± 18.3	TN
2018 Oct. 12	1.10	5950 ± 248	–	15.80 ± 0.52	4.24 ± 0.63	–	199.7 ± 12.3	280.1 ± 19.1	–	294.6 ± 12.8	296.5 ± 20.4	TN
2018 Oct. 14	1.12	4730 ± 247	11.00 ± 4.16	13.30 ± 0.52	3.90 ± 0.67	–	190.9 ± 25.7	–	–	234.0 ± 17.3	269.8 ± 20.5	TS
2018 Oct. 15	1.12	–	–	–	–	–	166.9 ± 18.3	257.9 ± 18.6	192.1 ± 21.2	226.1 ± 13.3	–	TS
2018 Oct. 18	1.14	–	–	–	–	–	151.0 ± 17.2	–	–	208.2 ± 12.4	230.8 ± 11.7	TS
2018 Oct. 18	1.14	–	–	10.80 ± 0.54	–	–	–	–	–	229.7 ± 14.3	–	TN
2018 Oct. 21	1.16	–	–	9.87 ± 0.51	3.02 ± 0.65	–	–	–	–	198.2 ± 19.4	–	TN
2018 Oct. 22	1.17	3500 ± 188		9.04 ± 0.50	2.30 ± 0.65	0.34 ± 0.21	137.6 ± 21.1	149.0 ± 26.1	–	114.4 ± 13.3	127.9 ± 14.4	TS
2018 Oct. 25	1.19	–	–	–	–	–	–	–	–	111.5 ± 20.0	–	TS
2018 Oct. 28	1.21	–	–	6.00 ± 0.55	–	–	–	151.2 ± 13.8	117.2 ± 16.5	137.6 ± 12.1	144.7 ± 14.1	TS
2018 Nov. 01	1.24	2320 ± 234	–	6.88 ± 0.56	–	–	–	108.1 ± 18.6	85.7 ± 23.6	109.6 ± 15.7	123.2 ± 12.4	TS
2018 Nov. 05	1.27	2010 ± 191	–	5.62 ± 0.52	1.16 ± 0.66	–	95.7 ± 20.4	120.5 ± 21.8	50.1 ± 16.2	121.1 ± 15.4	139.0 ± 15.0	TS
2018 Nov. 09	1.31	–	–	–	–	–	–	–	–	88.8 ± 13.4	129.3 ± 15.6	TS
2018 Nov. 14	1.35	–	–	4.39 ± 0.55	1.27 ± 0.69	–	85.5 ± 13.2	88.7 ± 18.7	87.2 ± 14.6	86.9 ± 13.6	91.3 ± 12.0	TS
2018 Dec. 07	1.55	–	–	3.30 ± 0.52	–	–	–	–	–	42.9 ± 10.5	71.7 ± 13.2	TS
2018 Dec. 10	1.58	–	–	3.00 ± 0.56	–	–	–	75.9 ± 14.2		28.1 ± 13.9	–	TS
2018 Dec. 19	1.66	–	–	3.30 ± 0.54	–	–	–	80.6 ± 12.5		27.2 ± 11.5	172.3 ± 18.2	TS
2018 Dec. 29	1.75	–	–	–	–	–	–	–	–	–	57.9 ± 18.1	TS
2019 Jan. 14	1.90	–	–	–	–	–	–	–	–	60.7 ± 11.1	–	TS
2019 Jan. 15	1.91	–	–	–	–	–	–	–	–	57.2 ± 11.0	60.4 ± 11.6	TS
2019 Jan. 29	2.04	–	–	–	–	–	–	–	–	85.5 ± 11.4	93.5 ± 11.5	TS
2019 Feb. 02	2.08	–	–	–	–	–	–	–	–	83.7 ± 12.5	91.6 ± 11.3	TS
2019 Feb. 04	2.10	–	–	–	–	–	–	–	–	71.5 ± 22.0	96.3 ± 17.1	TS

Notes. r_h is the heliocentric distance. The $A(0)f\rho$ values are printed at 10 000 km form the nucleus and corrected for the phase-angle effect.